International Journal of Mechanical Sciences 321 (2026) 111668

Contents lists available at ScienceDirect

International Journal of Mechanical Sciences

journal homepage: www.elsevier.com/locate/ijmecsci

In situ elucidation of fracture mechanisms governing crack transition to plasticity arrest

Abdalrhaman Koko [a,b,*], Bemin Sheen [c], Caitlin Green [a], Fionn Dunne [b]

[a] National Physical Laboratory, Hampton Road, Teddington TW11 0LW, United Kingdom
[b] Department of Materials, Royal School of Mines, Imperial College London, United Kingdom
[c] Department of Mechanical Engineering, Imperial College London, United Kingdom

ARTICLE INFO

Keywords:
Fracture mechanics
Elastoplastic deformation
Crack propagation
Process zone evolution
Energy release rate
SEM-based digital image correlation

ABSTRACT

Despite extensive theoretical treatment of short- to long-crack transitions, direct experimental quantification of how elastic and plastic energy contributions evolve at the crack tip during arrest has remained absent. In this study, we present an in situ investigation of crack propagation in cold-worked AA-5052 using high-resolution scanning electron microscopy digital image correlation (SEM-DIC) and electron backscatter diffraction (EBSD). By reconstructing local crack-tip fields from measured displacement data, we extract mode I and II stress intensity factors and both elastic and elastoplastic energy release rates (ΔJ_E and ΔJ_P). We show that microstructure-sensitive cracks propagate in a mixed-mode manner at low driving force and transition to a plasticity-dominated, load-aligned arrested state as the crack-tip process zone develops to span multiple grains. This transition is identified by the divergence of elastic and elastoplastic energy measures ($\Delta J_E \geq \Delta J_P$), together with crack-tip blunting, slip-band emission, and the emergence of localised plastic deformation. Under the present free-surface geometry and constraint conditions, these observations support the interpretation that crack arrest coincides with a measurable transition in crack-tip energy partitioning and correlates more directly with estimated surface process-zone expansion relative to the microstructure than with any single crack-length threshold.

1. Introduction

Crack propagation in structural metals remains a key concern in high-performance applications such as aerospace, marine, and transportation systems. Ensuring structural integrity over time depends not only on delaying crack initiation but also on understanding how cracks grow and, critically, how they might arrest [1,2]. Yet, in high-ductility alloys, such as cold-worked aluminium, crack behaviour is especially complex due to the interplay between residual plastic deformation and heterogeneous microstructures [3,4]. While long cracks are generally well-described by global fracture mechanics parameters, what is described in the literature as *short cracks* are not solely controlled by far-field applied stresses, but are substantially affected by interactions with the local microstructure [5–7], such as grain boundaries [8,9], intragranular misorientations [8,10], and residual stress distributions [11,12]. These interactions create highly variable crack growth rates and tortuous crack paths as the crack advances through individual grains [9,13,14]. These distinctions do not simply scale down from long-crack behaviour [15,16], and the common classification of cracks as ‘short’ or ‘long’ does not by itself indicate whether the fracture is dominated by microstructural interactions or by continuum-level driving forces.

This distinction becomes particularly important when predicting the transition from microstructure-sensitive crack growth to arrest in ductile materials, yet despite decades of fracture research, a continuous experimental picture of how cracks evolve from microstructure-sensitive paths to plasticity-dominated behaviour remains incomplete [17]. While ductile tearing is commonly accepted as the primary crack propagation mechanism [18–20], the mechanisms of microstructure-sensitive crack propagation and their transition to ductile tearing require further investigation. Most available studies either focus on long crack growth using global parameters such as K_{IC} or J_{IC} [21–23], or they examine microstructural crack-microstructure interactions in isolation [4, 24–27], either through post-mortem analysis [4,28,29], modelling [30–32], or discontinuous observations [33,34], often limited by spatial resolution or lacking full-field strain data [35–37]. Additionally, recent

* Corresponding author at: National Physical Laboratory, Hampton Road, Teddington TW11 0LW, United Kingdom.
E-mail address: abdo.koko@npl.co.uk (A. Koko).

https://doi.org/10.1016/j.ijmecsci.2026.111668
Received 15 February 2026; Received in revised form 6 April 2026; Accepted 26 April 2026
Available online 27 April 2026

high-resolution DIC studies of microstructurally small fatigue cracks under cyclic loading have further shown that even local crack-tip descriptors may lose simple proportionality to crack-growth response when strong strain localisation develops ahead of the crack tip, for example, when ΔCTOD deviates from its otherwise near-linear relation with crack growth rate because of local hardening and shear localisation [38,39]. Although these cyclic studies do not address monotonic crack arrest directly, they reinforce the broader point that crack-tip metrics in microstructure-sensitive regimes must be interpreted together with the evolving local deformation field rather than as standalone scalar descriptors.

While prior studies have addressed aspects of microstructure-sensitive crack growth and ductile tearing separately, and proposed that crack-tip plastic-zone development governs the transition from microstructure-sensitive to ductile crack behaviour, direct in situ quantification of crack-tip driving forces during this transition remains missing. This transition is crucial to both the scientific understanding of crack evolution and the engineering prediction of failure, particularly in FCC alloys where crack blunting and plastic shielding compete with surface formation. In this study, we directly address this missing link. Using in situ scanning electron microscopy-based digital image correlation (SEM-DIC) combined with electron backscatter diffraction (EBSD), we follow crack propagation in a cold-worked 5052 aluminium alloy (AA-5052) as the crack-tip process zone evolves from being confined within individual grains to spanning multiple grains, while EBSD provides the grain, subgrain, and boundary architecture against which crack deflection, boundary transfer, and early process-zone confinement are interpreted. This approach enables direct experimental quantification of crack-tip driving-force evolution as the process zone grows relative to the microstructure, allowing the observed transition to be interpreted in process-zone terms rather than by crack length alone.

The remainder of this paper is structured as follows. Section 2 describes the material, in situ SEM-DIC methodology, and displacement-driven reconstruction framework. Section 3 presents crack evolution and reconstructed fracture metrics. Section 4 discusses the transition from microstructure-sensitive propagation to plasticity-dominated arrest in terms of energy partitioning and process-zone development. Finally, the key findings and implications are summarised.

2. Methodology

This section describes the material, experimental configuration, and the displacement-driven reconstruction framework used to extract crack-tip driving forces. The methodology integrates in situ SEM-DIC measurements with EBSD characterisation and finite element reconstruction. The experimental measurements define the initial microstructural and evolving displacement fields, while the finite-element reconstruction uses these data to recover stress and energy measures consistent with the measured kinematics.

2.1. Material and pre-mechanical testing characterisation

An ASTM E647 compact tension (CT) specimen was fabricated from an aerospace-grade AA-5052 aluminium alloy plate with a rolling texture (see Fig. S3) and an average grain diameter of 31.7 ± 8.0 μm. The CT specimen's notch was aligned with the rolling direction. AA-5052 was selected as a model system due to its strain-hardened microstructure, high work-hardening rate, and relevance to ductile fracture in non-heat-treatable aluminium alloys [40–42]. These features make it ideally suited for studying plasticity-driven crack transition mechanisms in a controlled, well-characterised environment.

The chemical composition of the AA-5052 plate was confirmed using a HITACHI X-MET8000 Expert CG X-ray fluorescence (XRF) spectrometer to perform positive material identification. The detailed elemental composition results are presented in Table 1. In addition, the plate residual stresses were subsequently measured using the cos α method via Pulstec μ-X360 diffractometer with Cr-Kα radiation and a 0.3 mm pinhole collimator, achieving a spot size of approximately 1 mm, from a depth of around 10 μm at a 25° inclination.

Table 1
Measured chemical composition of the AA-5052 plate in weight %.

Al	Mg	Fe	Cr	Si	Mn	Cu	Zn
96.047 ± 0.255	3.137 ± 0.176	0.360 ± 0.009	0.223 ± 0.037	0.133 ± 0.020	0.050 ± 0.004	0.043 ± 0.004	0.007 ± 0.003

The specimen was prepared using precision wire electrical discharge machining to ensure dimensional accuracy and to minimise residual stresses introduced during the cutting process. The final geometry of the CT specimen featured a thickness (B) of 2.82 ± 0.02 mm, an effective width (W) of 13 ± 0.08 mm, notch length of 6.5 mm, and radius of 0.19 mm, with the pin diameter machined to 3.25 mm, as illustrated in Fig. 1a. The specimen was fatigue pre-cracked at a frequency of 10 Hz, with a load ratio (R) of 0.1, until a sharp crack of 76.42 ± 0.70 μm was achieved, as shown in Fig. 1c.

Following fatigue pre-cracking, the specimen was mechanically mirror-polished to remove any surface deformation, and the microstructure around the notch was mapped using EBSD performed with a Zeiss Auriga 60 SEM equipped with an Oxford Symmetry 2 EBSD detector. The specimen was positioned at a working distance (WD) of 14 mm from both the SEM pole piece and the EBSD detector. An electron beam with an accelerating voltage of 20 keV and a 120 μm aperture (yielding a beam current of approximately 10 nA) was employed for diffraction data collection at a step size of 0.5 μm. EBSD scans performed after polishing and before monotonic loading confirmed that the microstructure near the fatigue pre-crack tip remained consistent with the cold-worked state, with no signs of residual plasticity or substructure development (Fig. 3a).

For HR-EBSD analysis [43] of the sub-microstructure of the cold-rolled AA-5052, high-resolution 1244 × 1024-pixel Kikuchi patterns were collected with a 100-millisecond exposure per pattern and 50 nm step size. Subsequent EBSD analyses – including slip trace analysis – were performed using MTEX [44], and HR-EBSD analyses were performed using CrossCourt v4, with the patterns segmented into 40 regions before cross-correlation with a reference pattern, selected using the method described in [45], to estimate the local distribution of residual stresses and geometrically necessary dislocation (GND) density [46]. In addition to the EBSD analysis, the chemical composition of precipitates present in the microstructure was investigated using energy dispersive X-ray spectrometry (EDX) via an Oxford X-Max80 detector at an accelerating voltage of 10 kV and a WD of 5 mm.

Sequential EBSD mapping during crack propagation was not performed because the gold speckle pattern required for SEM-DIC precludes reliable diffraction acquisition. In addition, following the transition to plasticity-dominated behaviour, the high level of surface deformation resulted in substantial degradation of Kikuchi pattern quality, preventing quantitative extraction of post-deformation GND fields near the crack tip. Consequently, EBSD-derived metrics reported here characterise the initial microstructural state rather than dynamic crack-tip evolution, with EBSD defining the initial crystallographic orientation field, subgrain structure, and boundary character, which are used both to assign local anisotropic properties in the finite element reconstruction for the J-integral and stress intensity factors calculations, and to interpret how the crack path and early process zone interact with the measured microstructural heterogeneity. Additionally, serial sectioning 3D EBSD was attempted in the arrested crack region. However, the severe plastic deformation and lattice distortion within approximately 70–80 μm of the crack tip led to substantial degradation of Kikuchi pattern quality, preventing reliable orientation indexing in the immediate crack-front vicinity (see Fig. S8). As a result, quantitative GND

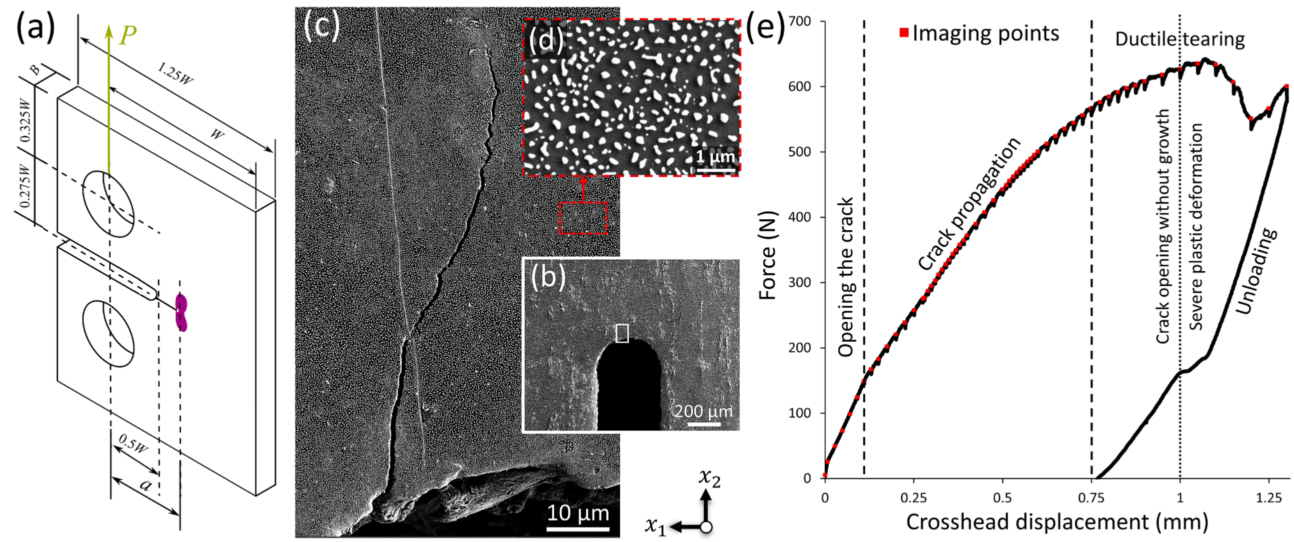

Fig. 1. Imaging and mechanical testing of the specimen. (a) Schematic of the ASTM E647 CT specimen geometry, showing key dimensions including specimen thickness (***B***), effective width (***W***), and notch configuration. The loading (***P***) direction is indicated by green arrows, with the other side fixed. (b) Low-magnification SEM image of the CT notch and pre-crack region. (c) Higher-magnification ETD-SEM image of the fatigue-induced crack tip area (white box in (b)). (d) ETD-SEM image of the gold nanoparticle speckle pattern used for DIC, with an average particle size of 225 ± 16 nm. (e) Nominal load-displacement curve, from the monotonic in situ SEM loading of the fatigue pre-cracked specimen, is segmented as observed via the SEM images. Red markers indicate the 61 imaging points where SEM snapshots were captured to correlate crack evolution with loading conditions. The unloading branch corresponds to post-arrest unloading after severe plastic deformation, not cyclic crack-growth testing.

evolution at the crack tip could not be extracted post-deformation.

2.2. Mechanical testing

The pre-cracked specimen was subjected to monotonic tensile loading within an Apreo S2 SEM to facilitate further propagation of the initial fatigue crack. The tensile test was conducted using a 5 kN Deben in situ tensile stage at a constant displacement rate of 0.1 mm/min. The specimen was positioned at a WD of 13.6 mm from the SEM pole piece, and imaging was performed using an electron beam at 5 kV and 1 nA.

The specimen was continuously monitored during the test, but the test was periodically paused under displacement control for 2 min to capture high-resolution images of the crack growth (red dots in Fig. 1e) using an Everhart-Thornley Detector (ETD) with a pixel size of 25.8 nm. The contrast between the high-density gold speckles, which appeared as bright spots (as shown in Fig. 1d), and the AA-5052 matrix was leveraged to facilitate subsequent DIC analysis for monitoring crack propagation.

Following the mechanical testing, the specimen was scanned using an Alicona InfiniteFocus optical microscope to generate a three-dimensional dataset of the region surrounding the notch. The scanning was performed with a 50x objective lens using an Alicona G5 model and processed using Alicona MeasureSuite software v.5.3.6.

2.3. Digital image correlation analysis

For SEM-DIC, a gold speckle pattern was applied to the specimen surface for high-resolution crack growth monitoring using SEM-DIC. A uniform 10 nm thick gold film was initially deposited onto the polished specimen using a Quorum Q150T coater at an accelerating voltage of 20 kV for 10 s. To achieve an optimal speckle pattern suitable for SEM-DIC analysis, a water vapour-assisted gold remodelling method [47,48] was employed for 6 h at 250 °C, facilitating the formation of discrete gold speckles with an average diameter of 225 ± 16 nm. This speckle size provided the necessary contrast and resolution to accurately monitor crack propagation during subsequent mechanical testing (Fig. 4).

Heating the specimen at 250 °C for 6 h, as part of the gold remodelling process, lies within the stress-relief annealing range for AA-5052 [49,50], which promotes dislocation recovery without recrystallisation, further reducing any residual stress introduced by the fatigue pre-crack.

DIC was employed to analyse the SEM images acquired during the in situ tensile testing. Before the DIC analysis, the images were aligned to a common field of view to eliminate rigid body movement, using the linear stack alignment plugin in Fiji ImageJ, leveraging the Scale-Invariant Feature Transform (SIFT) algorithm.

DIC data processing was conducted using DaVis v.10.2 software (LaVision GmbH). The analysis followed the best practices outlined in the iDICs guidelines [51]. Key parameters for the DIC process included a subset size of 17 pixels and a step size of 11 pixels, balancing spatial resolution and precision [52], and resulting in a displacement field with a 286 nm step size. The subset shape function was set to second order, enabling the capture of non-linear deformation fields around the crack tip. For image matching, the Zero-Normalised Sum of Squared Differences (ZNSSD) criterion was applied, offering robustness against intensity fluctuations and image noise, thereby enhancing correlation accuracy. A bicubic spline interpolant was used to generate smooth and continuous displacement fields, critical for precise strain mapping in regions of high deformation gradients. In addition, to correct for any residual rigid body movements, the method described in [53] was implemented. This approach involved identifying the point with the absolute minimum displacement within the image set and designating it as the origin.

2.4. J-integral and stress intensity factors calculations

We adopt a domain J-integral (ΔJ) formulation, computed between successive crack tip configurations based on full-field experimental displacement data from SEM-DIC. This avoids the need for stationary crack tip assumptions and instead directly quantifies the energy release and stress intensity factors (SIFs) during discrete crack advances. This approach is consistent with previous studies [54] that have used domain-integral methods with experimentally measured full-field displacement, including DIC [55,56], stereo-DIC [57,58], and even digital volume correlation [59,60].

Using a custom-made MATLAB script [61,62], a finite element (FE) model was created in Abaqus v.6.14 from the SEM-DIC field of view, excluding the crack geometry, to calculate the strain energy release rate and the mixed-mode SIFs at the crack tip, as shown in Fig. 2a and b. The model consisted of a rectangular grid composed of 4-node plane stress elements (Abaqus CPS4), designed to match the DIC grid, with no interpolation, ensuring a direct correlation between experimental and numerical data. Then, the experimentally measured DIC displacement field was applied as a boundary condition at each node in the FE model. Similarly, after registration of the EBSD data in MTEX, each element of the model's mesh is assigned an orientation by interpolating the orientations EBSD map at the location of each element centroid through inverse distance spatial interpolation.

In essence, the finite element framework is employed inversely: experimentally measured displacement fields are imposed as nodal boundary conditions, and the model reconstructs stress and energy fields consistent with these kinematics. It is not used to predict crack growth.

To calculate the elastic part of the strain energy release rate (ΔJ_{E}), we used AA-5052 anisotropic stiffness ($C_{11} = 106.75,\ C_{44} = 28.34,\ C_{12} = 60.41$ in GPa [63]) after it was transformed from the reference crystal coordinate system to the crystal orientation (or frame of reference) using a matrix ($\mathbf{g}$) constructed from the EBSD-determined Bunge-Euler angles (ϕ_1, Φ, ϕ_2) [64], as shown in question (1) to (4).

$$\mathbf{g}_Z(\phi_1) = \begin{bmatrix} \cos(\phi_1) & \sin(\phi_1) & 0 \\ -\sin(\phi_1) & \cos(\phi_1) & 0 \\ 0 & 0 & 1 \end{bmatrix}, \tag{1}$$

$$\mathbf{g}_{X'}(\Phi) = \begin{bmatrix} 1 & 0 & 0 \\ 0 & \cos(\Phi) & \sin(\Phi) \\ 0 & -\sin(\Phi) & \cos(\Phi) \end{bmatrix}, \tag{2}$$

$$\mathbf{g}_{Z''}(\phi_2) = \begin{bmatrix} \cos(\phi_2) & \sin(\phi_2) & 0 \\ -\sin(\phi_2) & \cos(\phi_2) & 0 \\ 0 & 0 & 1 \end{bmatrix}, \tag{3}$$

$$\mathbf{g}(\phi_1, \Phi,\ \phi_2) = \ \mathbf{g}_{Z''}(\phi_2)\ \mathbf{g}_{X'}(\Phi)\ \mathbf{g}_Z(\phi_1). \tag{4}$$

For an active rotation of the crystal axes in the sample reference frame, the rotation matrix (R) is used, where $\mathbf{R} = \mathbf{g}^T$. The rotated stiffness matrix ($\mathbf{C}'$) is then produced by rotating $\mathbf{C}$ as a 4th rank tensor, as expressed in Eq. (5). After rotation, $\mathbf{C}'$ is converted to a 6×6 2nd order tensor with Abaqus' ordering of the entries (leading diagonal: C_{11}, C_{22}, C_{33}, C_{12}, C_{13}, C_{23}).

$$\mathbf{C}' = \mathbf{R}{\cdot}\mathbf{R}{\cdot}\mathbf{C}{\cdot}\mathbf{R}^T{\cdot}\mathbf{R}^T, \tag{5}$$

$$C'_{ijkl} = R_{im}R_{jn}R_{kp}R_{lq}C_{mnpq}. \tag{6}$$

To account for nonlinearity and plastic deformation near the crack tip after the crack stopped growing, the full elastoplastic strain energy release rate (ΔJ_{P}) was calculated using the crystal-plasticity framework as implemented in [65], summarised here because it provides the constitutive basis for the plastic J-integral reconstruction. The mechanical part of the deformation gradient ($\mathbf{F}$) is decomposed multiplicatively into the elastic and plastic deformation gradients ($\mathbf{F}_e$ and $\mathbf{F}_p$ in Eq. (7)).

$$\mathbf{F} = \mathbf{F}_e\ \mathbf{F}_p. \tag{7}$$

The plastic velocity gradient ($\mathbf{L}_p$) is related to $\mathbf{F}_p$ and the rate of change of the plastic deformation gradient ($\dot{\mathbf{F}}_p$) as shown in (8). $\dot{\mathbf{F}}_p$ is expressed in terms of $\mathbf{F}_p$ at the start of a time increment, i.e., $(\mathbf{F}_p)_t$. Rearranging to equation allows $\mathbf{F}_p$ to be updated, based on $\mathbf{L}_p$, at the end of each increment.

$$\mathbf{L}_p = \dot{\mathbf{F}}_p\mathbf{F}_p^{-1} = \frac{\mathbf{F}_p - (\mathbf{F}_p)_t}{\Delta t}\mathbf{F}_p^{-1}, \tag{8}$$

$$\mathbf{F}_p = \left(\mathbf{I} - \mathbf{L}_p\Delta t\right)^{-1}(\mathbf{F}_p)_t, \tag{9}$$

where $\mathbf{L}_p$ is then obtained from the summation of shear rates on slip systems with slip direction ($\boldsymbol{s}$) and slip normal ($\boldsymbol{n}$). The slip rate on the α^{th} slip system, $\dot{\gamma}^a$ is calculated using the Orowan-based slip law given in Eq. (11) [66]:

$$\mathbf{L}_p = \sum_a \dot{\gamma}^a s^a \otimes n^a, \tag{10}$$

$$\dot{\gamma}^a = \rho_{\mathrm{m}}\nu(b^a)^2\exp\left(-\frac{\Delta F^a}{kT}\right)\sinh\left(\frac{\Delta V^a}{kT}\left(\tau^a - \tau_c^a\right)\right), \tag{11}$$

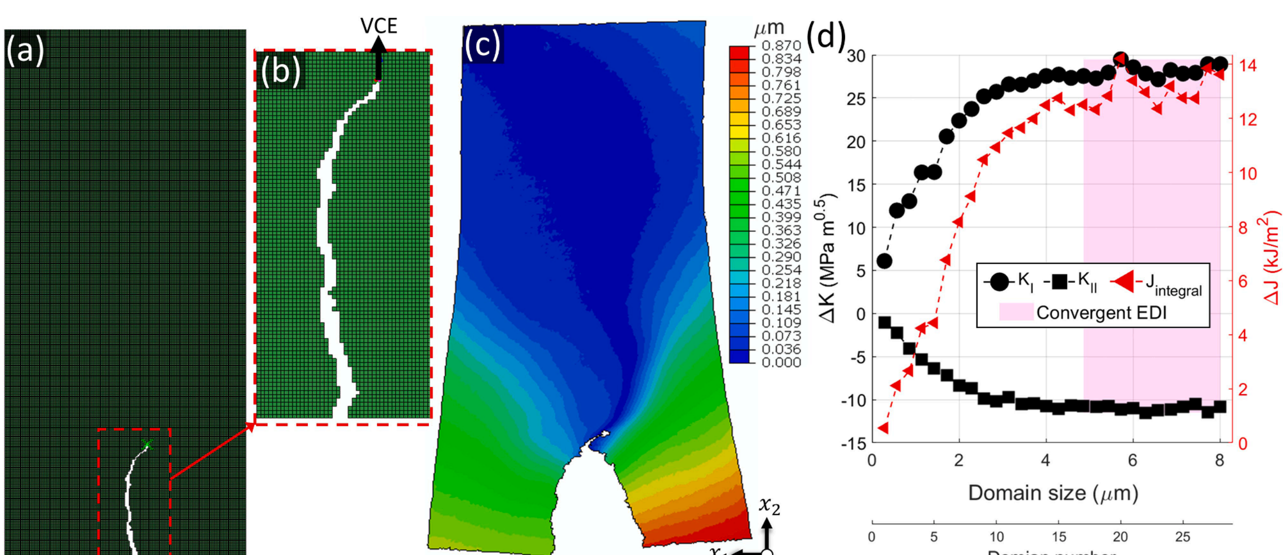

Fig. 2. Extraction of DIC-based SIFs. (a) A finite element mesh of the region of interest was created in Abaqus, replicating the experimental DIC field of view, with the physical crack geometry excluded from the mesh. (b) Zoomed view of the crack path, showing mesh refinement around the crack flanks and the virtual crack extension (VCE) direction used for J-integral evaluation. (c) Displacement magnitude in the deformed configuration after node-wise experimental DIC data were applied at 0.32 mm crosshead displacement. (d) Domain integral results for mode I (ΔK_{I}), mode II (ΔK_{II}), and the J-integral at 0.9 mm crosshead displacement. The shaded pink region marks the domain range used for extracting converged fracture parameters.

where k is the Boltzmann constant, T is the temperature, and τ is the resolved shear stress. The remaining constitutive parameters are listed in Table 2 and were adopted from published data for AA-5052 [67]. The activation volume is high to eliminate rate-dependent effects [68]. Accordingly, the magnitude of ΔJ_{p} depends on the chosen elastoplastic constitutive description, but this dependence is constrained here because the displacement field is imposed directly from experiment at each increment. Thus, the incremental J-integral formulation avoids assumptions of stationary crack-tip fields and allows direct evaluation of energy evolution during discrete crack advances.

To set the crystal orientation in the UMATs, the Euler angles in the Bunge convention of each material definition is required to be specified in its properties. As such, a material is defined for each element to model each orientation. It has been observed that more accurate results have been achieved by using a 3D mesh with UMATs compared to a 2D mesh. Accordingly, the model builds a mesh of C3D8 elements when using UMATs. Validation of this model can be found in the Supplementary Materials.

The elastic strain energy release rate (ΔJ_E) enabled the calculation of mode I (opening mode) and mode II (in-plane shear mode) SIFs at the crack tip using the interaction integral method implemented in Abaqus [69], which deconvolutes the forces acting on the crack. This dual approach allows us to identify the onset of plasticity-driven crack arrest by comparing ΔJ_{E} and ΔJ_{P}. For ΔJ_{E} and ΔJ_{P}, the equivalent domain integral (EDI) method [70] was coupled with the virtual crack extension (VCE) technique [71] to calculate the strain energy release rate, or the J-integral, per domain as the domain expanded from the crack tip in the VCE direction at 286 nm intervals. The VCE was set in the average direction that the crack took in the next interval, up to where the crack stopped growing, after which the crack was assumed to be parallel to the x_2-axis.

To further validate our approach, we examine the convergence behaviour of the domain integral with increasing domain size. As shown in the pink shaded area in Fig. 2d, the J-integral and stress intensity factors reach stable values over a well-defined domain region. This convergence confirms that the process zone is fully captured and that local unloading or DIC noise artefacts do not unduly affect the energy release rate. Initial non-convergence was attributed to the presence of highly localised plasticity [72,73] and insufficient strain data discretisation near the crack tip [74,75]. Variance within this region served as an indicator of convergence stability. Also, the sign of the mode II SIF is irrelevant, as it depends on the specific nodal arrangement at the crack tip and does not have a physical interpretation [76].

Comparatively, the CT specimen geometry and the crack length (L) was used to calculate the ASTM E1820 stress intensity factor (K_{ASTM}) per Eq. (12) [77], with its uncertainty calculated via the Monte Carlo method.

$$K_{ASTM} = \frac{P}{BW^{1/2}} \frac{2 + a/W}{(1 - a/w)^{3/2}} \left[0.886 + 4.64\left(\frac{a}{W}\right) - 13.32\left(\frac{a}{W}\right)^2 + 14.72\left(\frac{a}{W}\right)^3 - 5.6\left(\frac{a}{W}\right)^4 \right], \; a = 0.5W + L. \tag{12}$$

Table 2
AA-5052 properties used in Eq. (11).

Property	Symbol	Value	Units
Density of mobile dislocations	ρ_m	10^{12}	m^{-2}
Frequency of dislocation jumps	ν	10^{11}	s^{-1}
Magnitude of the Burgers vector	b	0.286	nm
Critical resolved shear stress	τ_c	65.74	MPa
Activation energy	ΔF	0.75	eV
Activation volume	ΔV	$400b^3$	m^3

3. Results

This section presents the evolution of crack morphology, strain fields, and reconstructed fracture metrics during monotonic loading. We first describe microstructure-sensitive crack propagation, followed by the transition to crack arrest and plasticity-dominated deformation.

3.1. Crack opening and propagation

As shown in Fig. 1e, the nominal load-displacement curve from the monotonic in situ test was divided into key regimes identified from the SEM images: initial crack opening, stable crack propagation, crack opening without growth, severe plastic deformation, and, after crack arrest, unloading. Further, the stable crack propagation regime was segmented with respect to its crystallographic orientation and grain boundary characteristics, as summarised in Table 3 and shown in Fig. 3a, allowing the observed crack deflections and transfer events to be related directly to the measured microstructural architecture. Overall, crack propagation was intragranular, starting in Grain A and terminating within Grain B, spanning 11 segments. Note that the word *intragranular* here is relative to our definition of grain boundaries at a 12° misorientation threshold.

In segment 1, the fatigue pre-crack opened fully at 149 N, followed by a minimal growth of 163 ± 6 nm and a more substantial extension of 3.00 ± 0.09 μm along the $(1\overline{1}\overline{1}) \pm 3.05°$ cleavage plane at applied 124 N and 0.09 mm. In this segment, DIC-based SIFs calculation showed a dominant mode I, with minimal mode II contribution, and the J-integral showed a steady linear increase until the crack opened and then proceeded with a steeper linear increase once the crack started growing into segments 2 and 3 (Fig. 5b).

In segment 2, the crack extended by 4.61 ± 0.30 μm under 183 N at 0.15 mm crosshead displacement, with propagation following a path between high local misorientations. This trend continued in segments 3 to 4, with extensions of 8.10 ± 0.01 μm and 4.59 ± 0.19 μm at 258 N and 312 N, respectively. In segments 2 to 4, EBSD indicates that these segments traverse a cold-worked subgrain structure containing low-angle boundaries, ranging between 1.5° and 4.5°, and orientation gradients, suggesting that early crack advance is guided by local compatibility variations and heterogeneous slip accommodation rather than by a homogeneous grain interior. High-resolution EBSD mapping of multiple regions across the specimen (Fig. 3b and c) reveals a cold-worked substructure with intense type III plastic deformation containing low-angle grain boundaries, dislocation walls, and relatively high geometrically necessary dislocation density. Although these maps were acquired away from the crack and therefore do not track dynamic evolution, they define the initial heterogeneity scale that likely underpins the observed crack deflections,

Table 3
Crystallographic tracing of the crack. Characteristics of the crack path in the AA-5052 as traced from SEM images and the EBSD map (Fig. 3a and Fig. 4a). Sections are shown in Fig. 3a. Crosshead displacement, in mm, and force, in N, tabulated below, are taken at the end of the segment.

Grain	no.	mm, N	Length (μm)	Crack plane
A	1	0.09, 124	0 (7.18 ± 0.09)	$(1\overline{1}\overline{1}) \pm 3.05°$
	2	0.15,183	4.61 ± 0.30	-
	3	0.25, 258	8.10 ± 0.01	-
	4	0.32, 312	4.59 ± 0.19	-
	5	0.35, 335	5.34 ± 0.02	$(\overline{1}\overline{2}1) \pm 3.30°$
Σ13 ± 2.76° grain boundary				
B	6	0.4, 372	18.83 ± 0.28	$(112) \pm 1.44°$
	7	0.45, 408	2.34 ± 0.16	$(\overline{1}2\overline{2}) \pm 0.84°$
	8	0.53, 462	8.28 ± 0.03	$(112) \pm 1.44°$
	9	0.57, 485	2.44 ± 0.24	$(\overline{1}2\overline{2}) \pm 2.49°$
	10	0.675, 536	2.34 ± 0.01	-
	11	0.75, 567	2.10 ± 0.12	$(11\overline{1}) \pm 1.65°$

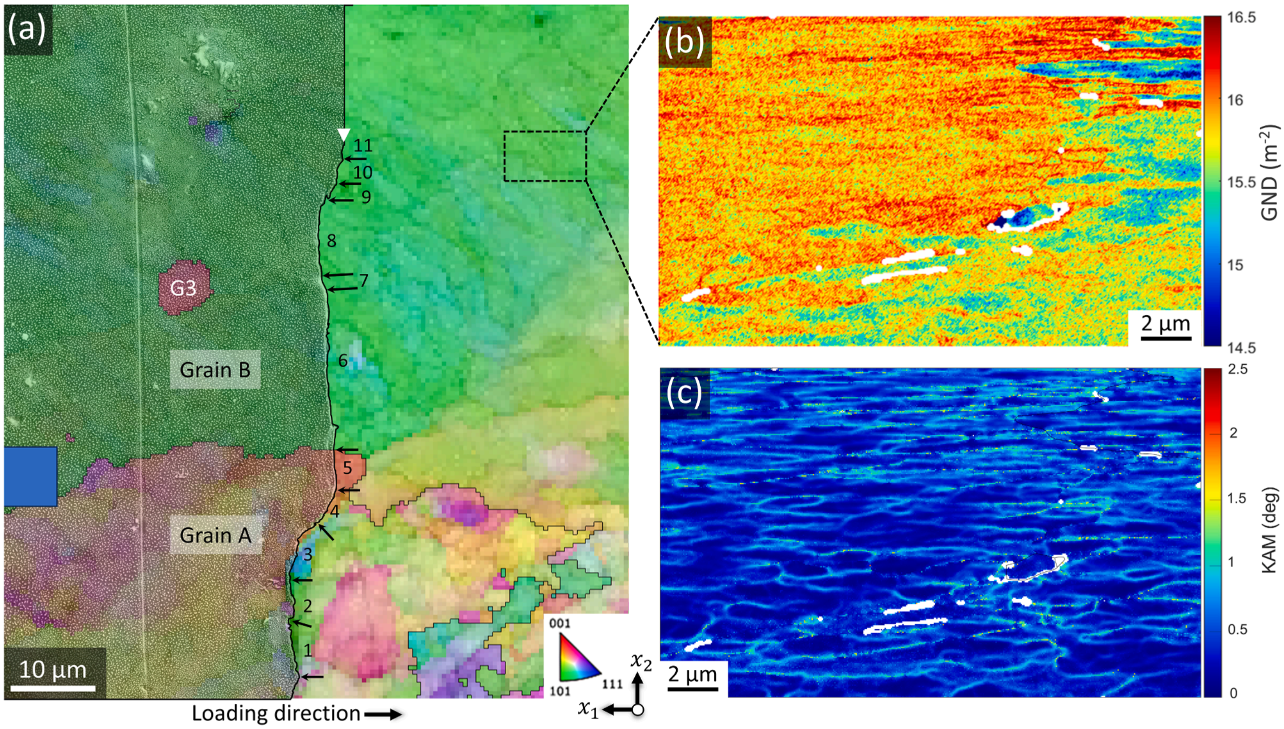

Fig. 3. AA-5052 microstructure. (a) EBSD orientation map acquired before testing using a 0.5 µm step size, with the stationary portion of the crack, recorded at 0.75 mm crosshead displacement, superimposed. The final crack path (taken from Fig. 4a) is superimposed here to illustrate how the crack interacted with the initial microstructure prior to deformation. Grains A and B are determined based on a 12° grain boundary misorientation threshold; using a lower threshold reveals subgrain structures indicative of cold work. (b) Geometrically necessary dislocation (GND) density map derived from high-resolution EBSD data acquired at a 50 nm step size. (c) Kernel average misorientation (KAM) map calculated using a 3-pixel window for the same field of view as B, highlighting local plastic strain gradients. The maps in B/C were collected away from the crack, as a general representative of the initial microstructure.

mixed-mode fluctuations, and confined early process-zone behaviour. Additionally, the X-ray measured residual type I elastic stress in the material is low, estimated at –20.50 ± 11.51 MPa, indicating that most of the deformation captured in the microstructure is plastic in nature. Notably, the linear increase in DIC-based mode I and the *J*-integral plateaued in segment 4, when the crack started to curve up to segment 5.

In segment 5, the crack followed the $(\bar{1}21) \pm 3.30°$ plane for 5.34 ± 0.02 µm, reaching an applied 335 N at 0.35 mm. At this point, the crack crossed into Grain B through a Σ13 ± 2.76° grain boundary. Analysis of the strain field and SEM imaging (Fig. 4b and c), interpreted together with the EBSD-identified Σ13 boundary in Fig. 3a, revealed that, while the crack tip continued to open steadily, it encountered localised resistance at the boundary, causing a visible deflection in its path. The ε_{11} strain field shows a marked concentration just before boundary crossing (0.28 – 0.31 mm crosshead displacement), which is redistributed upon entry into Grain B (0.34 – 0.37 mm crosshead displacement), consistent with local plastic accommodation during intergranular crack transfer. This transfer is also reflected in the DIC-based SIFs (Fig. 5b): mode II exhibited an increase approaching the boundary, while mode I remained dominant. The fluctuation in mode II suggests shear-driven deformation transfer, while the overall increase in the *J*-integral indicates an elevated energy requirement for intergranular propagation. Despite this, the crack advanced into Grain B after local strain redistribution at the boundary, indicating that in the present case, the identified Σ13 boundary did not prevent crack transfer.

In segment 6, the crack showed a marked increase in crack length to 18.83 ± 0.28 µm along the $(112) \pm 1.44°$ plane at applied 372 N and 0.40 mm. In segment 7, the crack path transitioned to the $(\bar{1}2\bar{2}) \pm 0.84°$ plane, extending 2.34 ± 0.16 µm at applied 408 N and 0.45 mm. In both segments, there was a gradual linear increase in DIC-based mode I and *J*-integral, while mode II plateaued, indicating forward propagation, primarily under mode I conditions.

As the crack approached a Fe-rich intermetallic precipitate (see Fig. S4 for chemical analysis), associated with common Al–Fe–Mn–Si compounds in AA-5xxx series alloys, it began to deviate from its prior trajectory. The SEM and strain field sequence (Fig. 4d and e) clearly illustrates how the crack tip manoeuvred around the precipitate between 0.5 mm and 0.56 mm crosshead displacement, accompanied by a redistribution of ε_{11} strain along the periphery of the particle and the strain localises along the new crack path, suggesting a surface-sensitive deviation driven by particle interaction and local plastic accommodation. During this segment, both DIC-based mode I and II SIFs (Fig. 5b) sharply decreased at 0.5 mm crosshead displacement, indicating a momentary reduction in crack driving force due to obstacle interaction.

In segment 8, the crack realigned with the $(112) \pm 1.44°$ plane and extended 8.28 ± 0.03 µm at nominal 462 N and 0.53 mm. The strain fields show a surface-driven crack path, influenced by stress intensification from the precipitate. The *J*-integral increased steadily throughout this segment, while DIC-based mode I and II, and the *J*-integral rose again. This behaviour suggests a recovery of crack propagation capacity after bypassing the precipitate, indicating resumed forward propagation under mixed-mode conditions.

In segment 9, the crack continued along $(\bar{1}2\bar{2}) \pm 2.49°$ for 2.44 ± 0.24 µm at nominal 485 N and 0.57 mm, and in segment 10, the crack exhibited non-crystallographic propagation over 2.43 ± 0.01 µm at nominal 536 N and 0.675 mm. Finally, in segment 11, the crack followed the $(11\bar{1}) \pm 1.65°$ plane for 2.1 ± 0.12 µm at nominal 567 N and 0.75 mm, where the crack terminated within Grain B after 63.65 ± 1.23 µm growth under displacement control (Fig. 4a). During segments 9 to 11, mode I and II, and the *J*-integral continue to increase, with mode I being dominant.

Overall, given the notch size, the ASTM-based SIF estimate (Fig. 5a and c) remained proportional to the applied load and insensitive to crack–microstructure interactions. In contrast, analysis of the in-plane displacement fields obtained from DIC enabled calculation of the local

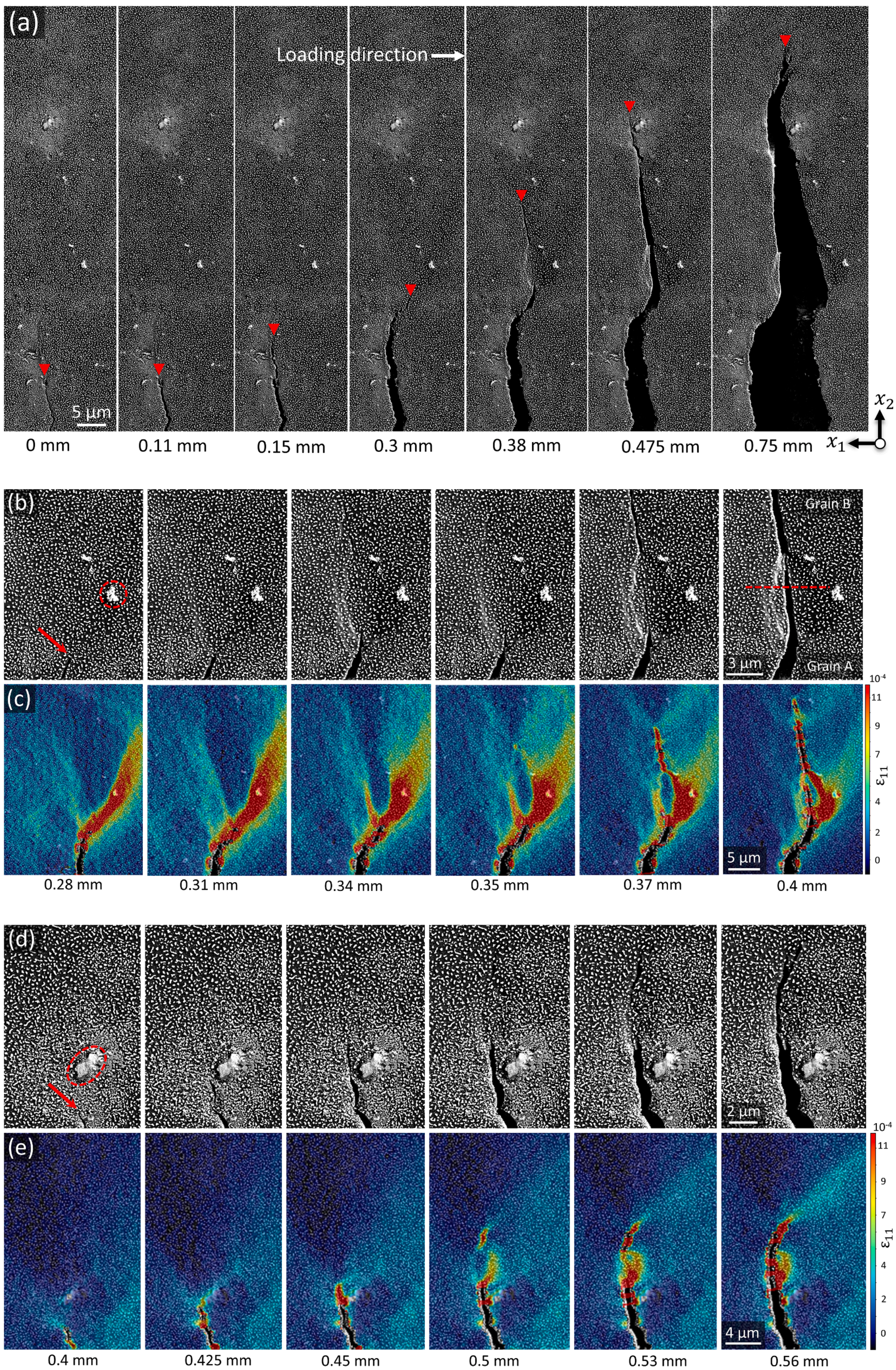

Fig. 4. SEM and DIC characterisation of the crack growth. (a) SEM image sequence showing the full progression of the crack from the initial fatigue pre-crack (0 mm) to its final length at 0.75 mm crosshead displacement. The red arrowheads track the advancing crack tip. (b) SEM image and (c) in-plane axial strain (ε_{11}) sequence showing crack propagation from Grain A into Grain B across a Σ13 grain boundary. The red arrow indicates the advancing crack tip, while the dashed circle highlights the Fe-rich precipitate. (d) SEM image and (e) in-plane axial strain (ε_{11}) sequence showing the crack tip interaction with a Fe-rich precipitate (see Fig. S4 for chemical analysis) during the transition from segment 7 to segment 8. For the strain field during crack propagation, see Movie S1.

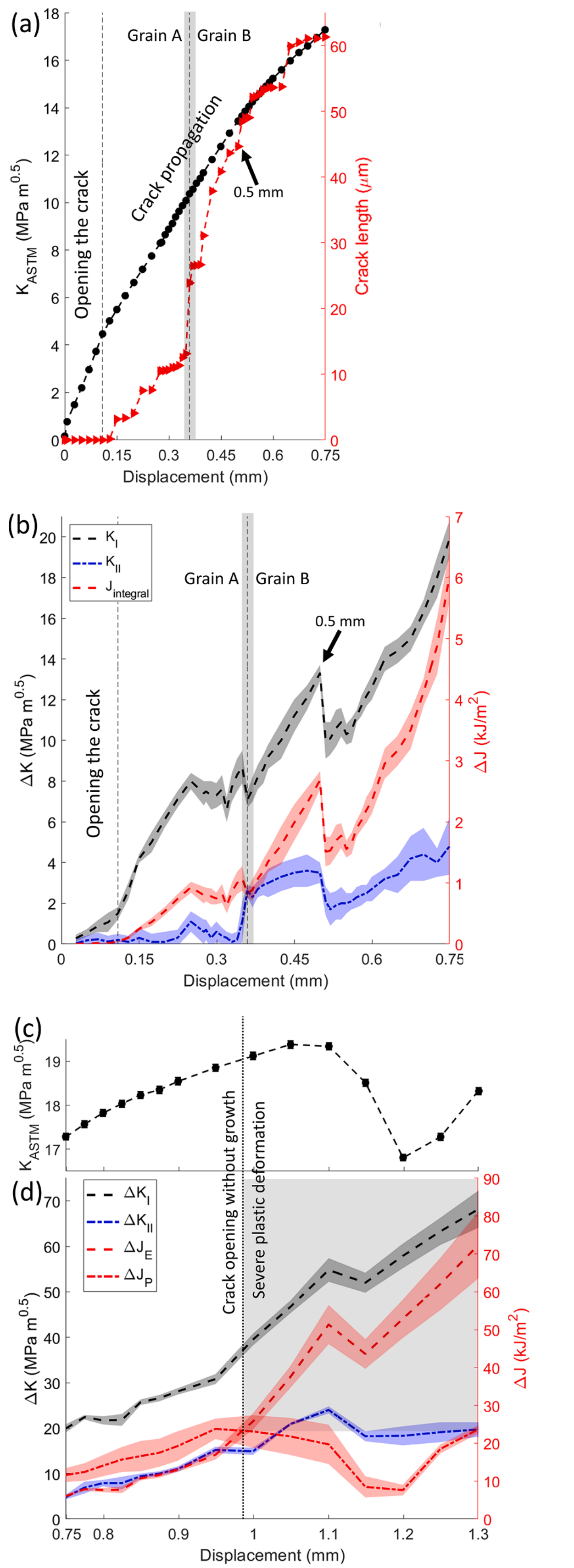

(caption on next column)

Fig. 5. Crack stress intensity factors and strain energy release rate. (a) ASTM-based mode I SIF (K_{ASTM}, black) plotted against displacement, alongside measured crack growth (red, right axis) up to when the crack stopped growing, as defined from Fig. 4a. (b) DIC-based fracture metrics, including mode I (black), mode II (blue), and strain energy release rate (ΔJ, red, right axis) plotted against crosshead displacement for initial crack opening and stable crack propagation regimes. (c) K_{ASTM} and (d) DIC-derived fracture metrics, including both elastic (ΔJ_E) and elastoplastic (ΔJ_P) components of the strain energy release rate (red, right axis), for crack opening without growth and severe plastic deformation regimes, as defined in Fig. 1a. Shaded bands around plotted curves represent domain-wise variability in fracture metrics (ΔJ, ΔK_I, and ΔK_{II}) calculated using the EDI method. These are derived from the converged integration region (see pink shaded area in Fig. 2d) and reflect standard visualisation of convergence spread in DIC-based analysis. The grey shaded region in D marks the regime beyond 0.984 ± 0.011 mm crosshead displacement, where the elastic assumptions of linear fracture mechanics break down. See Fig. S5 for the combined figures of A and C, as well as B and D.

strain energy release rate (J-integral) and mode-separated SIFs along the crack path, with the J-integral and the decoupled mode I and II exhibiting strong sensitivity to local microstructural conditions and corresponding well with the observed crack growth.

3.2. Ductile tearing

Beyond 0.75 mm crosshead displacement, further displacement resulted in a crack opening but with no further propagation. From SEM images (Fig. 6a), two distinct regimes were identified: one where the crack opened with no apparent plasticity, and another where pronounced plastic deformation became apparent, evidenced by the formation of slip bands emitted from the crack tip. While initial visual inspection suggested this transition occurred at a crosshead displacement of 1 mm; quantitative analysis identified the transition as the first loading increment at which (i) crack length remained constant under increasing displacement and (ii) the divergence between the J-integrals – calculated using elastic properties to extract mode I and II (i.e., ΔJ_E) and the J-integral calculated using elastoplastic properties (i.e., ΔJ_P) – revealed a more accurate transition point at 0.984 ± 0.011 mm crosshead displacement and 23.28 ± 2.81 kJ/m^2 (Fig. 5d).

Note that the small differences visible between ΔJ_E and ΔJ_P at ~0.75 mm displacement reflect methodological and numerical factors rather than actual plasticity, because inverse crystal plasticity solutions are inherently more sensitive to measurement noise and convergence behaviour than purely elastic reconstructions, which affects J-integral convergence (see the larger variability in Fig. 5d compared to the elastic case) and leads to minor deviations in calculated stress and energy fields even for elastically responding cracks (Supplementary Information, Section 1). Thus, the divergence between ΔJ_E and ΔJ_P becomes physically meaningful only after crack arrest, when plastic deformation develops, as shown in Fig. 5d Beyond ~0.7 mm and up to the convergence region, ΔJ_E and ΔJ_P exhibit similar trends, although ΔJ_P aligns more closely with K_{ASTM} (based on applied load). This reinforces that ΔJ_P only gains physical significance after crack arrest, coinciding with the onset of plasticity.

The observed divergence in the energy measures is consistent with the visual onset of severe plastic deformation at the crack tip and indicates the stage at which purely elastic mode I and II interpretations become progressively less reliable. However, beyond 0.984 mm crosshead displacement, using elastic properties beyond this point has shown – qualitatively – that mode I remains dominant and is increasing, while mode II plateaued, signalling a regime shift from mixed-mode microstructure-sensitive crack to mode I (load)-dominated crack. In contrast, the elastoplastic J-integral (ΔJ_P) began to plateau with applied displacement, reflecting the onset of severe plastic deformation, and matching the nominal force behaviour, including the force drop around 1.2 mm (Fig. 1e). Because the test was conducted under displacement control, this load drop reflects a reduction in structural stiffness

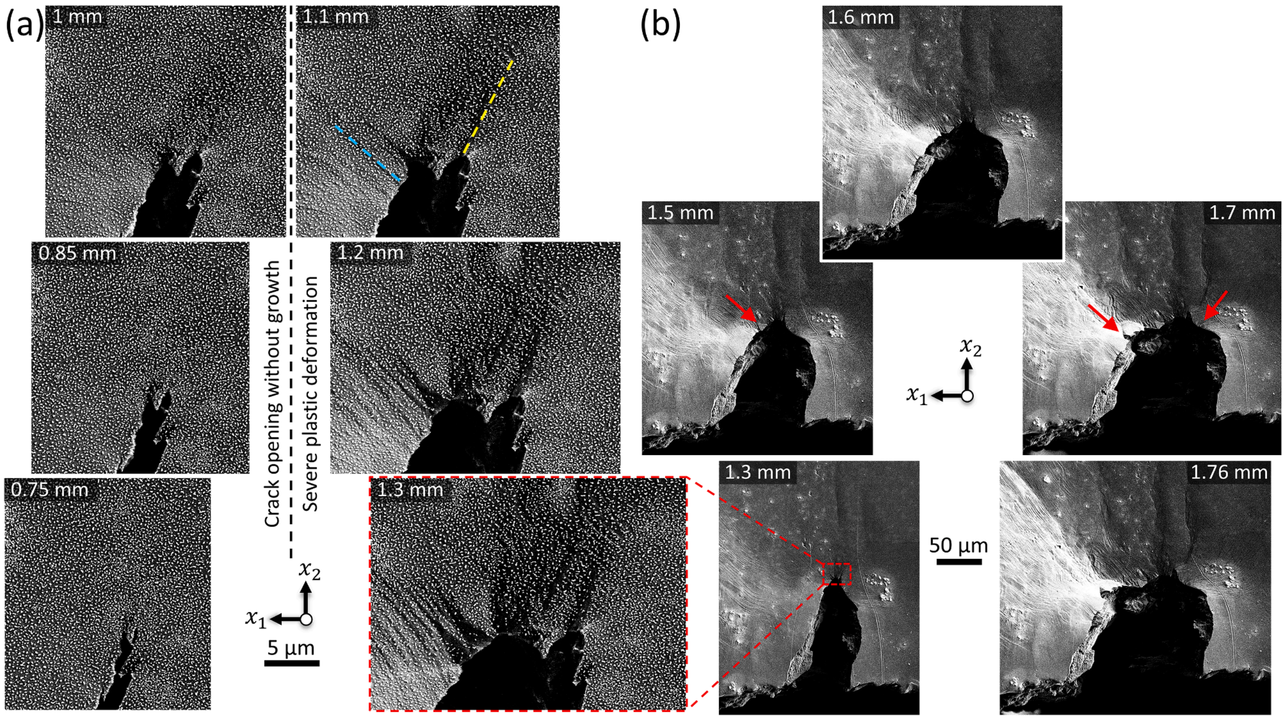

Fig. 6. Plasticity development at the crack tip. (a) SEM sequence showing crack behaviour from final propagation (0.75 mm) through to severe plastic deformation (1.3 mm). The yellow and blue dashed lines are $(1\bar{1}\bar{1})[0\bar{1}1]$ and $(\bar{1}1\bar{1})[0\bar{1}\bar{1}]$ slip trace, respectively (b) Wider field SEM views show continued deformation from 1.3 mm to 1.8 mm crosshead displacement. Red arrows indicate ductile tearing and localised surface shear.

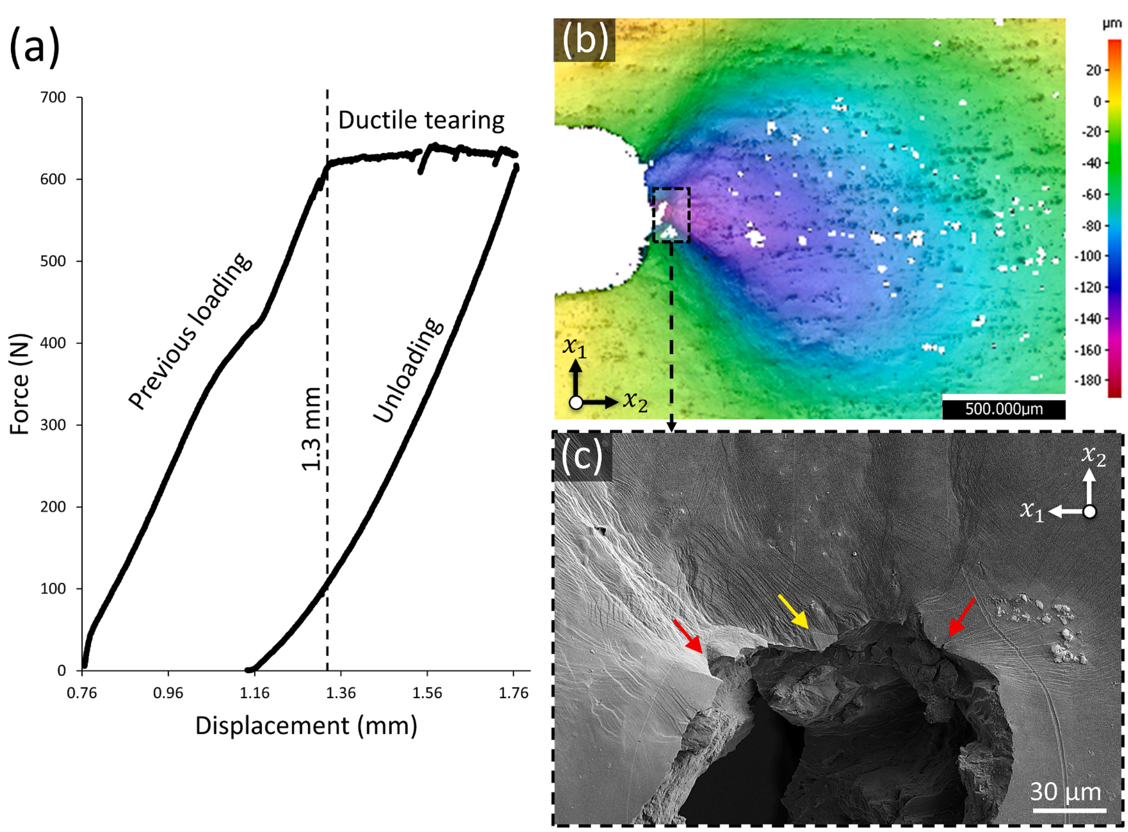

Fig. 7. Localised plasticity at the crack tip. (a) The nominal load-displacement curve was recorded during reloading after crack arrest. (b) 3D topography map of the post-arrest crack region. (c) High-resolution SEM image of the same region. Red arrows denote sites of ductile tearing where secondary cracks nucleated, while the yellow arrow highlights a region where intersecting slip bands and localised contrast features suggest the possible formation of a sessile Lomer dislocation lock. Arrows are spatially correlated with the features identified in Fig. 6b.

associated with the onset of plastic deformation near the arrested crack tip. At this stage, the crack ceases to grow, and the surrounding material begins to yield, leading to a localised structure softening.

As displacement increases, initially $(1\bar{1}\bar{1})[0\bar{1}1]$ (yellow dashed line) and $(\bar{1}1\bar{1})[0\bar{1}\bar{1}]$ (blue dashed line in Fig. 6a) slip bands radiated from the crack tip and blunting initiates, forming a plastic stretch zone. After 1.3 mm of crosshead displacement, the crack was unloaded as shown in Fig. 1e, with the crack remaining open at 0.766 mm crosshead displacement. The crack was then loaded again (Fig. 7a), and despite continued crosshead displacement from 1.3 mm to 1.76 mm, the load plateaued around 640 N, indicating crack arrest under severe plastic strain conditions, absorbing the applied energy rather than contributing to further elastic stress buildup. In addition, as crosshead displacement increased, slip band formation and ductile tearing emerged, particularly beyond 1.5 mm (highlighted by red arrows in Fig. 6b). The crack tip blunted into a rounded geometry, and the surrounding surface developed an elliptical singularity, suggesting the development of a stretch zone and plasticity-dominated blunting. These features align with macro-scale crack opening, indicating irreversible energy dissipation via plastic flow, and confirm the shift to opening-mode-controlled deformation in a macroscale plastic regime. The crack remained open upon unloading, confirming substantial residual strain and irreversible deformation in the surrounding matrix.

Thus, the divergence between ΔJ_E and ΔJ_P is interpreted here as an experimental signature of a shift from microstructure-sensitive crack propagation toward a plasticity-dominated regime, in which increasing displacement is accommodated progressively more by local yielding and crack-tip blunting than by further crack propagation. This is a hallmark of ductile fracture, and its onset aligns with the plateau in mode II contribution as the crack aligns with the principal stress direction, with crack arrest corresponding to full ligament yielding before crack advance as a long crack, where global loading and plastic dissipation – not microstructural barriers – govern the fracture response.

Further evidence of plasticity-driven fracture behaviour after crack arrest is revealed by the topography and high-magnification SEM imaging in Fig. 7c showing the blunted crack tip and extensive plastic surface features, including slip steps and shear bands. The 3D surface height map (Fig. 7b) shows an elliptical depression centred at the crack tip and approximately 180 μm deep at its centre, extending ahead of the arrested crack tip, and indicates continued localised plastic deformation and stretch-zone formation at the free surface under near-plane-stress conditions. This residual deformation confirms that, after crack arrest, applied energy is dissipated through local plastic flow rather than further crack advance, consistent with the SEM-DIC strain-field evolution.

4. Discussion

The central physical result of this study is not the observation that ductile cracks eventually arrest due to plasticity, which is well established, but the direct experimental quantification of how the crack-tip driving force evolves during this transition. By reconstructing both elastic and elastoplastic energy measures from the same measured displacement fields, we show that crack arrest is accompanied by a measurable change in the balance between recoverable elastic response and plastic dissipation associated with crack blunting. This transition is identified through changes in energy partitioning and correlates with observed slip-band emission and process-zone expansion; within the present experiment, it is not explained by a unique crack length alone. The contribution of the present work is therefore the experimental linkage between crack-tip field evolution and the onset of plasticity-dominated arrest under controlled microstructural conditions.

4.1. Microstructure-sensitive crack propagation

AA-5052 is a non-heat-treatable alloy that relies on solid solution strengthening and strain hardening rather than precipitation hardening [41,42]. In this alloy with pronounced microstructural plasticity, the crack initially propagated through a pre-existing subgrain-dislocation structure, which is likely to generate heterogeneous local compatibility stresses and uneven slip transfer. However, at this length scale and with 286 nm spatial resolution, the crack exhibited a quasi-brittle surface response, propagating along non-cleavage planes with limited observable plasticity and minimal crack-tip blunting. Here, ‘quasi-brittle’ refers only to the early surface-observed crack response, namely crack advance with highly localised deformation, limited observable surface plasticity, and minimal crack-tip blunting, despite the alloy’s overall ductile behaviour under monotonic loading. Strain fields remained highly localised at the crack tip but confined to a small process zone ahead of the crack.

Together, the EBSD crack tracing and SEM-DIC fields indicate that early crack propagation is governed by the interaction between microstructural heterogeneity, local plastic accommodation, and the evolving stress state, rather than by crystallographic orientation alone. Although dynamic GND evolution at the crack tip could not be measured, the initial EBSD and HR-EBSD maps define a subgrain heterogeneity scale comparable to the early process-zone size inferred from SEM-DIC. Mixed-mode fluctuations observed in Fig. 5b are therefore interpreted as arising from local compatibility stresses and uneven slip accommodation imposed by that pre-existing subgrain structure.

While mode I – the principal loading mode – remains the dominant fracture mechanism throughout the microstructure-sensitive crack growth, mode II contributions become non-negligible in segments where the crack interacts with grain boundaries and precipitates, with possible mode III contributions that cannot be resolved experimentally. Comparatively, ASTM-based SIF estimates scaled with load and ignored microstructural effects, while DIC-derived *J*-integrals and mode-separated SIFs were highly sensitive to local microstructure and aligned with crack growth behaviour. Nonetheless, during the microstructure-sensitive crack growth, the ASTM and DIC-based SIFs analysis reveals that the crack propagated at a stress intensity factor substantially lower than the typical fracture toughness range reported for AA-5052 (25–30 MPa·m$^{0.5}$ [78]).

4.2. Microstructure-sensitive to load-dominated crack transition

As the crack stopped growing, the transition from quasi-brittle to plasticity-dominated crack behaviour was governed primarily by surface-local phenomena, as evidenced by SEM-DIC strain fields and the development of a crack-tip plastic zone from initial blunting and surface slip-band formation (Fig. 6a) to the evolving surface topography (Fig. 7b), such that additional applied energy is dissipated through plastic flow rather than crack advance, prior to the onset of plasticity-dominated blunting and ductile tearing (Fig. 7c). These observations are typical characteristics of crack arrest in ductile alloys under monotonic loading [19,22,79].

Traditionally, microstructure-sensitive crack propagation in ductile alloys at low energy has often been discussed in terms of crack length effects [65,80,81] (i.e., short crack), whereas a substantial theoretical body of work also emphasises the controlling role of crack-tip process-zone development and plastic shielding [82,83]. In the present experiments, when the process zone was small, the crack interacts with subgrain microstructure, promoting quasi-brittle, crystallographic facet growth even in otherwise ductile materials (e.g., cleavage-like facets in AA-5052 [79]). As the *J*-integral increases, the process zone expands to engage multiple grains and activates mechanisms such as slip-band interaction, crack deflection, and microvoid coalescence. Consistent with process-zone-based interpretations of microstructure-sensitive crack behaviour, the transition observed here coincides with the process zone reaching a critical extent, rather than being captured by a unique crack length alone.

In this view, the transition toward plasticity-dominated arrest is identified by the divergence between the elastic and elastoplastic energy measures extracted from the same displacement fields, occurring over the same loading range as crack arrest and the first clear signs of crack-tip blunting and slip-band activity (Fig. 4a). This divergence is a consequence of the present analysis framework: the same measured SEM-DIC displacement field is imposed in both reconstructions, but only the elastoplastic formulation can relax stress through plastic flow. (demonstrated further in Fig. S6b). Because the present analysis is based on incremental J-integral values, this divergence reflects the transition from energy being available for crack advance to energy being dissipated through plastic deformation. Accordingly, the observed divergence between ΔJ_E and ΔJ_P, i.e. ΔJ_{crit} when $\Delta J_E \geq \Delta J_P$, can be interpreted as a physically consistent indicator of the transition toward plasticity-dominated crack arrest. Furthermore, the mechanistic basis of ΔJ_{crit} is supported by direct physical observations: visible slip bands initiate ahead of the tip (Fig. 6a), the crack blunts (Fig. 6b), and a growing plastic zone develops (Fig. 7b and c). However, its numerical value is conditional on the present material state, microstructure, geometry, and constraint conditions, and should therefore be interpreted as an experimentally observed transition indicator for crack arrest under the present conditions rather than as a universal material parameter.

The present observations can be interpreted in light of process-zone-based perspectives, such as the Kysar framework [83], which emphasises the competition between energy dissipation by new surface formation and by dislocation-mediated blunting at the crack tip. Here, the spatiotemporal evolution of the process zone (Movie S1) shows strain fields progressively radiating from the crack tip under increasing displacement, highlighting gradual enlargement of the plastically deforming region, particularly as the crack arrests. The SEM-DIC-based ΔK_I, ΔK_{II}, and ΔJ therefore provide physically grounded, surface-resolved measures of the crack-tip field that act as practical scalars for process-zone development at the free surface.

Mathematically, for material under plane stress and light to moderate strain hardening, the process zone size (r_p, visualised in Fig. 8) can be estimated from the J-integral using [84]:

$$r_p \approx \frac{2}{\pi}\frac{J}{\sigma_0} \tag{13}$$

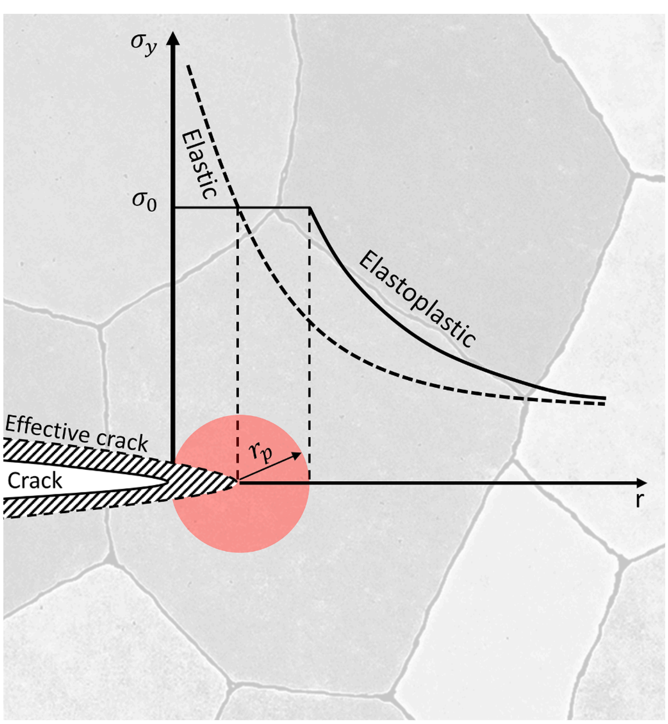

Fig. 8. Visualisation of the process zone and effective crack length at the grain-scale level for a microstructure-sensitive crack.

In our study, uniaxial tensile testing of a similarly cold-worked and textured AA-5052 specimen yielded a 0.2 % offset yield stress (σ_0) of 193 MPa (see Supplementary Fig. S6a). Using this value in Eq. (13), the experimentally identified transition value, $\Delta J_{crit} = 23.28 \pm 2.81$ kJ/m^2, corresponds to a process-zone size on the order of 76.8 ± 9.3 µm at the observed transition. Notably, this process zone spans more than twice the average grain size of the material, which was measured at 31.7 ± 8.0 µm. This dimensional comparison supports the interpretation that, once the plastic zone spans multiple microstructural heterogeneities, the influence of individual GND-rich regions diminishes, and crack behaviour becomes increasingly load-dominated. Notably, this dimension closely matches the radial extent of the unindexed region observed in serial sectioning 3D EBSD of the arrested crack (Fig. S8e), where severe lattice distortion prevented reliable orientation reconstruction. The spatial agreement between the energetically estimated process-zone size and the diffraction-degraded volume provides independent structural support for the interpretation that crack arrest coincides with intense plastic strain localisation spanning multiple grains. While evolving GND accumulation at the crack tip was not directly measured, the observed slip-band emission and large strain gradients (Fig. 6) confirm that plastic strain localisation surpasses the initial stored deformation state at this stage.

Moreover, although the initial pre-crack was relatively large, 76.42 ± 0.70 µm, it still exhibited microstructure-sensitive crack behaviour following stress-relief annealing. Under the present free-surface geometry and near-plane-stress constraint conditions, the observed transition therefore correlates more directly with the estimated surface process-zone development than with any single crack-length threshold. Once the process zone expanded to engage multiple grains, fracture behaviour became less sensitive to grain-scale heterogeneity and more nearly load-dominated. This supports the use of plasticity-sensitive descriptors derived from measured crack-tip fields, alongside length-based metrics such as Δa, when interpreting crack resistance in ductile alloys. Similar process-zone-related transitions have been reported in aluminium [22,79,85], titanium [34], Ni-based superalloys [86], and steels [87,88], although further studies across FCC systems with varying hardening responses and microstructures are needed to assess the broader generality of the present ΔJ_{crit}-based transition framework.

Nonetheless, it is worth noting that the present process-zone estimates are derived from surface-resolved displacement fields and therefore reflect the free-surface response under plane stress conditions. Subsurface plasticity and through-thickness constraint may evolve differently and could contribute to the overall crack-front driving force. While the surface transition identified here coincides with crack arrest under the tested geometry and thickness, full three-dimensional characterisation would be required to determine how this transition scales with thickness and constraint. The present conclusions, therefore, pertain to the experimentally accessible surface process zone rather than to a fully three-dimensional crack-front field.

4.3. Cautionary note on J-integral applicability

It is important to distinguish between ΔJ values extracted during active crack growth and those obtained after crack arrest. During crack propagation, crack-tip deformation remains localised and surface dominated, justifying the use of surface-resolved fracture metrics to characterise the transition. After crack arrest, extensive plastic deformation develops and through-thickness constraint effects become significant. ΔJ values extracted in this post-arrest regime are therefore surface specific and are used here only to indicate the breakdown of elastic assumptions, the transition from mixed-mode microstructure-sensitive crack to mode I (load) governed crack, and the onset of plasticity-dominated blunting (Fig. 5d), rather than to represent crack-front driving forces. Additionally, although the J-integral is an appropriate metric for studying microstructure-sensitive cracks, its validity in elastoplastic materials requires that the integration domain fully encloses the plastic zone [72,89,90]. Its successful application in this study relies on the near-homogeneous elastic anisotropy of the grains, with stiffness differences below 3 %, which minimised the influence of grain misorientation.

More generally, the physical meaning of the *J*-integral at the micro-scale remains weakly demonstrated [15]. The present results show that it can provide a meaningful measure of the crack-tip field when plasticity anisotropy is effectively homogeneous, consistent with prior work in anisotropic single-phase materials [91–93]. Caution is required when extending this approach to polycrystalline systems with strong elastic or plastic anisotropy or sharp interfaces, where path independence may break down and interaction- or interface-integral formulations will be required [94–98].

While such approaches are well developed numerically, in situ experimental validation at the micro-scale remains constrained, especially for three-dimensional measurements. Existing synchrotron-based techniques, such as Laue micro-diffraction [99], differential aperture X-ray microscopy [100], and dark-field X-ray microscopy [101], are limited to elastic strains and post-mortem analysis, and volumetric correlation methods lack the necessary spatial resolution. As a result, surface-based SEM-DIC remains one of the few practical experimental approaches for resolving free-surface crack-tip mechanics during microstructurally sensitive short-crack propagation in aluminium alloys.

5. Conclusion

This work provides direct, high-resolution experimental evidence of how fracture in cold-worked AA-5052 transitions from microstructure-sensitive crack growth to plasticity-dominated arrest. By integrating SEM-DIC and EBSD with crystal plasticity finite element modelling, we quantified local crack-tip fields and extracted elastic and elastoplastic energy release rates (ΔJ_E, including mode I and II, and ΔJ_P) from measured displacement data.

Our findings show that, in the present material and geometry, the observed transition is more clearly associated with the evolution of the crack-tip process zone relative to the microstructure than with crack length alone. When the process zone remains confined within a single grain, crack growth is mixed-mode and highly sensitive to local heterogeneities. As loading increases and the process zone expands to span multiple grains, the response becomes increasingly plasticity-dominated, microstructural constraints diminish, and the crack aligns more closely with the macroscopic stress direction. The transition is identified by divergence between elastic and elastoplastic energy measures ($\Delta J_E \geq \Delta J_P$), coincident with crack-tip blunting, slip-band formation, and ductile tearing.

The numerical value of the transition energy is specific to the present material state and to the surface-resolved response measured by SEM-DIC under the present specimen geometry and free-surface constraint conditions. Nevertheless, the methodology enables direct quantification of this transition and provides a framework for investigating its dependence on microstructure and loading.

Funding

This work was supported by the National Measurement System (NMS) programme of the UK Department for Science, Innovation and Technology (DSIT), and the Royal Society Short Industrial Fellowship (SIF\R2\242,005).

Data and materials availability

All data needed to evaluate the conclusions in the paper are present in the paper and the Supplementary Materials. Raw and processed datasets generated during the current study are available from the corresponding author on reasonable request. The MATLAB-based toolbox used in this study is available under an MIT license at https://github.com/Shi2oon/DIC2ABAQUS.

CRediT authorship contribution statement

Abdalrhaman Koko: Writing – original draft, Visualization, Methodology, Investigation, Funding acquisition, Formal analysis, Conceptualization. **Bemin Sheen:** Writing – original draft, Validation, Software. **Caitlin Green:** Visualization, Investigation. **Fionn Dunne:** Writing – review & editing, Supervision, Resources.

Declaration of competing interest

The authors declare that they have no known competing financial interests or personal relationships that could have appeared to influence the work reported in this paper.

Acknowledgement

We thank Ms Rachel Willia (National Physical Laboratory) for the XRD measurements, Duaa Salim (University of Khartoum) for validating crack length measurements, Dr Ken Mingard (National Physical Laboratory) for reviewing the manuscript, and Professor James Marrow (University of Oxford) and Elsiddig Elmukashfi (University of Leicester) for the insightful discussions, which enhanced the quality of the article.

Supplementary materials

Supplementary material associated with this article can be found, in the online version, at doi:10.1016/j.ijmecsci.2026.111668.

References

[1] Sénac C. Mechanisms and micromechanics of intergranular ductile fracture. Int J Solids Struct 2024;301:112951. https://doi.org/10.1016/j.ijsolstr.2024.112951.
[2] Yang A, Liu YJ, Wang C, Gao Y, Chen P, Ju H, et al. Enhanced grain boundary cohesion mediated by solute segregation in a dilute Mg alloy with improved crack tolerance and strength. Int J Plast 2024;176:103950. https://doi.org/10.1016/j.ijplas.2024.103950.
[3] Noell PJ, Sills RB, Benzerga AA, Boyce BL. Void nucleation during ductile rupture of metals: a review. Prog Mater Sci 2023;135:101085. https://doi.org/10.1016/j.pmatsci.2023.101085.
[4] Huang R, Zhou Y, Yang Q, Yang X, Wei K, Qu Z, et al. Localized brittle intergranular cracking and recrystallization-induced blunting in fatigue crack growth of ductile tantalum. Int J Plast 2025;186:104262. https://doi.org/10.1016/j.ijplas.2025.104262.
[5] Wan W, Dunne FPE. Microstructure-interacting short crack growth in blocky alpha zircaloy-4. Int J Plast 2020;130:102711. https://doi.org/10.1016/J.IJPLAS.2020.102711.
[6] Liu Z, Dash SS, Zhang J, Lyu T, Lang L, Chen D, et al. Fatigue crack growth behavior of an additively manufactured titanium alloy: effects of spatial and crystallographic orientations of α lamellae. Int J Plast 2024;172:103819. https://doi.org/10.1016/j.ijplas.2023.103819.
[7] Guo G, Zhang W, Zhang B, Xu J, Chen S, Ye X, et al. Effect of precipitate phase on the plastic deformation behavior of alloy 718: in-situ tensile experiment and crystal plasticity simulation. Int J Plast 2025;187:104286. https://doi.org/10.1016/j.ijplas.2025.104286.
[8] Ren P, Withers PJ, Zuo Z, Feng H, Huang W. Microstructural effects on short fatigue crack propagation in cast Al-Si alloys. Int J Fatigue 2023;175:107788. https://doi.org/10.1016/j.ijfatigue.2023.107788.
[9] Li J, Huang Q, Wang Z, Zhang N, Chen G, Qian G. Microstructural insights into fatigue short crack propagation resistance and rate fluctuation in a Ni-based superalloy manufactured by laser powder bed fusion. Int J Plast 2023;171:103800. https://doi.org/10.1016/j.ijplas.2023.103800.
[10] Fang J, Zhu Z, Zhang X, Xie L, Huang Z. Tensile deformation and fracture behavior of AA5052 aluminum alloy under different strain rates. J Mater Eng Perform 2021;30:9403–11. https://doi.org/10.1007/S11665-021-06112-5/METRICS.
[11] Smudde CM, D'Elia CR, San Marchi CW, Hill MR, Gibeling JC. The influence of residual stress on fatigue crack growth rates of additively manufactured type 304L stainless steel. Int J Fatigue 2022;162:106954. https://doi.org/10.1016/j.ijfatigue.2022.106954.
[12] Gao Z, Gan J, Liu H, Liu X, Wu W. Fatigue crack growth prediction for shot-peened steel considering residual stress relaxation. Mater Des 2023;234:112301. https://doi.org/10.1016/j.matdes.2023.112301.
[13] McDowell DL, Dunne FPE. Microstructure-sensitive computational modeling of fatigue crack formation. Int J Fatigue 2010;32:1521–42. https://doi.org/10.1016/j.ijfatigue.2010.01.003.
[14] Prithivirajan V, Ravi P, Naragani D, Sangid MD. Direct comparison of microstructure-sensitive fatigue crack initiation via crystal plasticity simulations

and in situ high-energy X-ray experiments. Mater Des 2021;197:109216. https://doi.org/10.1016/J.MATDES.2020.109216.
[15] Wilson D, Dunne FPE. A mechanistic modelling methodology for microstructure-sensitive fatigue crack growth. J Mech Phys Solids 2019;124:827–48. https://doi.org/10.1016/j.jmps.2018.11.023.
[16] Chen B, Jiang J, Dunne FPE. Is stored energy density the primary meso-scale mechanistic driver for fatigue crack nucleation? Int J Plast 2018;101:213–29. https://doi.org/10.1016/J.IJPLAS.2017.11.005.
[17] Kramer S., Boyce B., Jones A., Gearhart J., Salzbrenner B. The Sandia Fracture challenge: how ductile failure predictions fare, 2019, p. 25–9. https://doi.org/10.1007/978-3-319-95879-8_6.
[18] Zhao G, Sun M, Li J, Li H, Ma L, Li Y. Study on quasi-in-situ tensile microstructure evolution law of 5052-O aluminum alloy based on EBSD. Mater Today Commun 2022;33:104572. https://doi.org/10.1016/j.mtcomm.2022.104572.
[19] Espeseth V, Morin D, Tekoğlu C, Børvik T, Hopperstad OS. Ductile tearing of aluminium plates: experiments and modelling. Int J Fract 2023;242:39–70. https://doi.org/10.1007/s10704-023-00701-2.
[20] Ma L, Deng Y, Ren Y, Hu W. Influence of orientation on crack propagation of aluminum by molecular dynamics. Eur Phys J B 2022;95:25. https://doi.org/10.1140/epjb/s10051-022-00285-1.
[21] Lomakin IV, Mäkinen T, Widell K, Savolainen J, Coffeng S, Koivisto J, et al. Fatigue crack growth in an aluminum alloy: avalanches and coarse graining to growth laws. Phys Rev Res 2021;3:L042029. https://doi.org/10.1103/PhysRevResearch.3.L042029.
[22] Gattu M, Aala S. Size-effect method to determine mode-I fracture toughness of aluminium alloys. Eng Fract Mech 2021;242:107504. https://doi.org/10.1016/j.engfracmech.2020.107504.
[23] Paysan F, Melching D, Breitbarth E. Plasticity-induced crack closure identification during fatigue crack growth in AA2024-T3 by using high-resolution digital image correlation. Int J Fatigue 2025;192:108703. https://doi.org/10.1016/j.ijfatigue.2024.108703.
[24] Hu J, Zhuang Z, Liu F, Liu X, Liu Z. Investigation of grain boundary and orientation effects in polycrystalline metals by a dislocation-based crystal plasticity model. Comput Mater Sci 2019;159:86–94. https://doi.org/10.1016/j.commatsci.2018.12.010.
[25] Huang YC, Hou YC, Chang L, Yan T. An ex-situ study on epitaxial growth of nickel on copper substrate in electrodeposition. ECS Trans 2017;80:713–21. https://doi.org/10.1149/08010.0713ecst.
[26] Anh GN, Hütter G, Kuna M. Micromechanical modeling of crack initiation and propagation in the ductile-brittle transition region. Key Eng Mater 2016;713:58–61. https://doi.org/10.4028/www.scientific.net/KEM.713.58.
[27] Carroll JD, Abuzaid W, Lambros J, Sehitoglu H. High resolution digital image correlation measurements of strain accumulation in fatigue crack growth. Int J Fatigue 2013;57:140–50. https://doi.org/10.1016/j.ijfatigue.2012.06.010.
[28] Long DJ, Dunne FPE. On the mechanistic driving force for short fatigue crack path. J Mech Phys Solids 2023;179:105368. https://doi.org/10.1016/j.jmps.2023.105368.
[29] Wang K, Song K, Xin R, Zhao L, Xu L. Cyclic microstructure analysis, crack propagation and life prediction of Inconel 750H considering the slip fracture energy. Int J Plast 2023;167:103660. https://doi.org/10.1016/j.ijplas.2023.103660.
[30] Seiler M, Linse T, Hantschke P, Kästner M. An efficient phase-field model for fatigue fracture in ductile materials. Eng Fract Mech 2020;224:106807. https://doi.org/10.1016/j.engfracmech.2019.106807.
[31] Zan XD, Guo X, Weng GJ. Simulation of fracture behaviors in hydrogenated zirconium alloys using a crystal plasticity coupled phase-field fracture model. Int J Plast 2025;188:104304. https://doi.org/10.1016/j.ijplas.2025.104304.
[32] Xu Q, Pan K, Chen Y, Zhang Z. Anisotropic phase-field crystal plasticity modelling of fracture in nickel-based superalloy. Int J Plast 2025;190:104368. https://doi.org/10.1016/j.ijplas.2025.104368.
[33] Jiang J, Yang J, Zhang T, Dunne FPE, Britton TB. On the mechanistic basis of fatigue crack nucleation in Ni superalloy containing inclusions using high resolution electron backscatter diffraction. Acta Mater 2015;97:367–79. https://doi.org/10.1016/j.actamat.2015.06.035.
[34] Wang X, Cao M, Zhao Y, He J, Guan X. Microstructural causes and mechanisms of crack growth rate transition and fluctuation of additively manufactured titanium alloy. Int J Plast 2024;179:104034. https://doi.org/10.1016/j.ijplas.2024.104034.
[35] Cai W, Sun C, Wang C, Qian L, Fu MW. In-situ experiment and numerical modelling of the intragranular and intergranular damage and fracture in plastic deformation of ductile alloys. Int J Plast 2025;185:104217. https://doi.org/10.1016/j.ijplas.2024.104217.
[36] Li J, Huang Q, Wang Z, Zhang N, Chen G, Qian G. Microstructural insights into fatigue short crack propagation resistance and rate fluctuation in a Ni-based superalloy manufactured by laser powder bed fusion. Int J Plast 2023;171:103800. https://doi.org/10.1016/j.ijplas.2023.103800.
[37] Long DJ, Wan W, Dunne FPE. The influence of microstructure on short fatigue crack growth rates in Zircaloy-4: crystal plasticity modelling and experiment. Int J Fatigue 2023;167:107385. https://doi.org/10.1016/j.ijfatigue.2022.107385.
[38] Remes H, Romanoff J, Lillemäe I, Frank D, Liinalampi S, Lehto P, et al. Influence of microstructural deformation mechanisms and shear strain localisations on small fatigue crack growth in ferritic stainless steel. Int J Fatigue 2022;163:107024. https://doi.org/10.1016/j.ijfatigue.2016.11.019.
[39] Tillikainen I, Gallo P, Lehto P, Remes H. Study of cyclic crack-tip opening displacement of microstructurally small fatigue crack using digital image correlation. Fatigue Fract Eng Mater Struct 2023;46:4103–18. https://doi.org/10.1111/ffe.14124.
[40] Davis JR. Aluminum and aluminum alloys. ASM International; 1993.
[41] Li Y, Li L, Nie J, Cao Y, Zhao Y, Zhub Y. Microstructural evolution and mechanical properties of a 5052 Al alloy with gradient structures. J Mater Res 2017;32:4443–51. https://doi.org/10.1557/JMR.2017.310/METRICS.
[42] Soysal T, Kou S. Solidification cracking test of aluminium alloy 5052. Sci Technol Weld Join 2022;27:301–8. https://doi.org/10.1080/13621718.2022.2051410.
[43] Wilkinson AJ, Meaden G, Dingley DJ. High-resolution elastic strain measurement from electron backscatter diffraction patterns: new levels of sensitivity. Ultramicroscopy 2006;106:307–13. https://doi.org/10.1016/j.ultramic.2005.10.001.
[44] Bachmann F, Hielscher R, Schaeben H. Grain detection from 2d and 3d EBSD data—Specification of the MTEX algorithm. Ultramicroscopy 2011;111:1720–33. https://doi.org/10.1016/j.ultramic.2011.08.002.
[45] Koko A, Tong V, Wilkinson AJ, Marrow TJ. An iterative method for reference pattern selection in high-resolution electron backscatter diffraction (HR-EBSD). Ultramicroscopy 2023;248. https://doi.org/10.1016/j.ultramic.2023.113705.
[46] Wilkinson AJ, Randman D. Determination of elastic strain fields and geometrically necessary dislocation distributions near nanoindents using electron back scatter diffraction. Philos Mag 2010;90:1159–77. https://doi.org/10.1080/14786430903304145.
[47] Di Gioacchino F, Quinta da Fonseca J. Plastic strain mapping with sub-micron resolution using digital image correlation. Exp Mech 2013;53:743–54. https://doi.org/10.1007/s11340-012-9685-2.
[48] Di Gioacchino F, Quinta da Fonseca J. An experimental study of the polycrystalline plasticity of austenitic stainless steel. Int J Plast 2015;74:92–109. https://doi.org/10.1016/j.ijplas.2015.05.012.
[49] Mugendiran V, Gnanavelbabu A, Ramadoss R. Tensile behaviour of Al5052 alloy sheets annealed at different temperatures. Adv Mat Res 2013;845:431–5. https://doi.org/10.4028/www.scientific.net/AMR.845.431.
[50] Ravindran R, Manonmani K, Narayanasamy R. Effect of annealing on formability and crystallographic textures of aluminium 5052 alloy sheets. Int J Mater Res 2010;101:877–86. https://doi.org/10.3139/146.110347.
[51] Bigger R., Blaysat B., Boo C., Grewer M., Hu J., Jones A., et al. A good practices guide for digital image correlation. 2018. https://doi.org/10.32720/idics/gpg.ed1.
[52] Glushko O. A simple and effective way to evaluate the accuracy of digital image correlation combined with scanning electron microscopy (SEM-DIC). Results Mater 2022;14:100276. https://doi.org/10.1016/j.rinma.2022.100276.
[53] Mostafavi M, Collins DM, Cai B, Bradley R, Atwood RC, Reinhard C, et al. Yield behavior beneath hardness indentations in ductile metals, measured by three-dimensional computed X-ray tomography and digital volume correlation. Acta Mater 2015;82:468–82. https://doi.org/10.1016/j.actamat.2014.08.046.
[54] Becker TH. Extracting fracture properties from digital image and volume correlation displacement data: a review. Strain 2023. https://doi.org/10.1111/str.12469.
[55] Atkinson D, Becker T. A 117 line 2D digital image correlation code written in MATLAB. Remote Sens 2020;12:2906. https://doi.org/10.3390/RS12182906.
[56] Koko A, Earp P, Wigger T, Tong J, Marrow TJ. J-integral analysis: an EDXD and DIC comparative study for a fatigue crack. Int J Fatigue 2020;134:105474. https://doi.org/10.1016/j.ijfatigue.2020.105474.
[57] Koko A, Becker TH. Mixed-mode fracture: combination of Arcan fixture and stereo-DIC. Theor Appl Fract Mech 2024:104724. https://doi.org/10.1016/j.tafmec.2024.104724.
[58] Molteno MR, Becker TH. Mode I-III decomposition of the J -integral from DIC displacement data. Strain 2015;51:492–503. https://doi.org/10.1111/str.12166.
[59] Marrow J, Scotson D, Jin X, Chen H, Chen Y, Koko A, et al. Small-specimen testing, with image-based analysis, for crack propagation resistance in polygranular nuclear graphite. Graphite testing for nuclear applications: the validity and extension of test methods for material exposed to operating reactor environments. In: ASTM international100 Barr harbor drive, PO Box C700, West Conshohocken, PA 19428-2959; 2022. p. 1–17. https://doi.org/10.1520/STP163920210051.
[60] Koko A, Singh S, Barhli S, Connolley T, Vo NT, Wigger T, et al. 3-Dimensional analysis of fatigue crack fields and crack growth by in situ synchrotron X-ray tomography. Int J Fatigue 2023;170:107541. https://doi.org/10.1016/j.ijfatigue.2023.107541.
[61] Koko A, Marrow J. DIC2Abaqus: calculating mixed-mode stress intensity factors from 2D and 3D-stereo displacement fields. SoftwareX 2025;31:102231. https://doi.org/10.1016/j.softx.2025.102231.
[62] Koko A, Abdelnour A, Becker TH, Marrow TJ. Bridging experiments and defects' mechanics: a data-driven toolbox for configurational force analysis. Eng Comput 2026;42:21. https://doi.org/10.1007/s00366-025-02262-5.
[63] Crystal Structures. Second edition. Interscience Publishers, New York note: aluminum cubic closest packed structure. Cryst Struct, 1; 1963. p. 7–83.
[64] Salvati E, Sui T, Korsunsky AM. Uncertainty quantification of residual stress evaluation by the FIB–DIC ring-core method due to elastic anisotropy effects. Int J Solids Struct 2016;87:61–9. https://doi.org/10.1016/j.ijsolstr.2016.02.031.
[65] Dunne FPE, Rugg D, Walker A. Lengthscale-dependent, elastically anisotropic, physically-based hcp crystal plasticity: application to cold-dwell fatigue in Ti alloys. Int J Plast 2007;23:1061–83. https://doi.org/10.1016/j.ijplas.2006.10.013.
[66] Gibbs GB. Thermodynamic analysis of dislocation glide controlled by dispersed local obstacles. Mater Sci Eng 1969;4:313–28. https://doi.org/10.1016/0025-5416(69)90026-3.

[67] Hu P, Liu Y, Zhu Y, Ying L. Crystal plasticity extended models based on thermal mechanism and damage functions: application to multiscale modeling of aluminum alloy tensile behavior. Int J Plast 2016;86:1–25. https://doi.org/10.1016/j.ijplas.2016.07.001.
[68] Zhang Z. Micromechanistic study of textured multiphase polycrystals for resisting cold dwell fatigue. Acta Mater 2018;156:254–65. https://doi.org/10.1016/j.actamat.2018.06.033.
[69] Yu H, Kuna M. Interaction integral method for computation of crack parameters K–T – a review. Eng Fract Mech 2021;249:107722. https://doi.org/10.1016/j.engfracmech.2021.107722.
[70] Nikishkov GP, Atluri SN. Calculation of fracture mechanics parameters for an arbitrary three-dimensional crack, by the 'equivalent domain integral' method. Int J Numer Methods Eng 1987;24:1801–21. https://doi.org/10.1002/nme.1620240914.
[71] Parks DM. The virtual crack extension method for nonlinear material behavior. Comput Methods Appl Mech Eng 1977;12:353–64. https://doi.org/10.1016/0045-7825(77)90023-8.
[72] Shi MX, Huang Y, Gao H. The J-integral and geometrically necessary dislocations in nonuniform plastic deformation. Int J Plast 2004;20:1739–62. https://doi.org/10.1016/J.IJPLAS.2003.11.013.
[73] Meindlhumer M, Alfreider M, Sheshi N, Hohenwarter A, Todt J, Rosenthal M, et al. Resolving the fundamentals of the J-integral concept by multi-method in situ nanoscale stress-strain mapping. Commun Mater 2025;6:35. https://doi.org/10.1038/s43246-025-00752-z.
[74] Wawrzynek PA, Carter BJ, Banks-Sills L. The M-integral for computing stress intensity factors in generally anisotropic materials. MD: Hanover; 2005.
[75] Koko A, Elmukashfi E, Karamched PS, Marrow TJ. Computation of displacements from strain fields: derivation, validation, and application. Acta Mater 2026;304:121818. https://doi.org/10.1016/j.actamat.2025.121818.
[76] Courtin S, Gardin C, Bézine G, Ben Hadj Hamouda H. Advantages of the J-integral approach for calculating stress intensity factors when using the commercial finite element software ABAQUS. Eng Fract Mech 2005;72:2174–85. https://doi.org/10.1016/j.engfracmech.2005.02.003.
[77] ASTM E1820-18: Test method for measurement of fracture toughness 2025. https://doi.org/10.1520/E1820-25.
[78] Liu AF. Mechanical properties data for selected aluminum alloys. Mechanics and mechanisms of fracture: an introduction, materials park. Ohio: ASM International; 2005. p. 397–409.
[79] Koko A, Salim D, Leung N, Spetseiris N, Smith S, England D, et al. Exploring short crack behaviour and fracture transition in 5052 aluminium alloy. Results Eng 2025:105303. https://doi.org/10.1016/j.rineng.2025.105303.
[80] Krupp U, Düber O, Christ HJ, Künkler B, Köster P, Fritzen CP. Propagation mechanisms of microstructurally short cracks—factors governing the transition from short- to long-crack behavior. Mater Sci Eng: A 2007;462:174–7. https://doi.org/10.1016/j.msea.2006.03.159.
[81] Sadananda K, Nani Babu M, Vasudevan AK. A review of fatigue crack growth resistance in the short crack growth regime. Mater Sci Eng A 2019;754:674–701. https://doi.org/10.1016/J.MSEA.2019.03.102.
[82] Rice JR, Thomson R. Ductile versus brittle behaviour of crystals. Philos Mag J Theor Exp Appl Phys 1974;29:73–97. https://doi.org/10.1080/14786437408213555.
[83] Kysar JW. Energy dissipation mechanisms in ductile fracture. J Mech Phys Solids 2003;51:795–824. https://doi.org/10.1016/S0022-5096(02)00141-2.
[84] Hutchinson JW. Crack-tip singularity fields in nonlinear fracture mechanics: a survey of current status. Advances in fracture research. Elsevier; 1982. p. 2669–84. https://doi.org/10.1016/B978-0-08-025428-9.50015-2.
[85] Dong S, Tao Y, Han L, Wang H, Zhao J. Thickness-dependent micro-fracture behaviors of pre-cracked aluminum plates by crystal plasticity finite element method and damage criteria. Eng Fract Mech 2024;307:110285. https://doi.org/10.1016/j.engfracmech.2024.110285.
[86] Li J, Wang Z, Zhang N, Shi T, Gilbert EP, Chen G, et al. Crack-tip plasticity mediated grain refinement and its resisting effect on the fatigue short crack growth. Int J Plast 2024;181:104102. https://doi.org/10.1016/j.ijplas.2024.104102.
[87] Huang W, Peng H, Liu Y, Chen Y, Wu Y, Liu F, et al. Microstructure evolution and crack initiation behavior of Q450NQR1 high-strength weathering steel in very high cycle fatigue regime. Int J Fatigue 2024;185:108366. https://doi.org/10.1016/j.ijfatigue.2024.108366.
[88] Sahu JK, Krupp U, Christ HJ. Fatigue crack initiation behavior in embrittled austenitic–ferritic stainless steel. Int J Fatigue 2012;45:8–14. https://doi.org/10.1016/j.ijfatigue.2012.06.018.
[89] Theocaris PS. A comparison between the elastic strain energy and the plastic work at the crack tip. Eng Fract Mech 1988;30:767–77. https://doi.org/10.1016/0013-7944(88)90138-5.
[90] Kuang JH, Chen YC. The values of J-integral within the plastic zone. Eng Fract Mech 1996;55:869–81. https://doi.org/10.1016/S0013-7944(96)00077-X.
[91] Koko A, Becker TH, Elmukashfi E, Pugno NM, Wilkinson AJ, Marrow TJ. HR-EBSD analysis of in situ stable crack growth at the micron scale. J Mech Phys Solids 2023;172:105173. https://doi.org/10.1016/j.jmps.2022.105173.
[92] Su X, Zhang Z, Williamson M, Vuksic M, Koko A, Marrow TJ. Measurement of cleavage toughness of brittle materials by local elastic field analysis. Acta Mater 2026;304:121797. https://doi.org/10.1016/j.actamat.2025.121797.
[93] Su X, Wan W, Koko A, Dunne FPE, Marrow TJ. Crack field analysis by optical DIC of short cracks in Zircaloy-4. Procedia Struct Integr 2022;39:663–70. https://doi.org/10.1016/j.prostr.2022.03.139.
[94] Simha NK, Fischer FD, Kolednik O, Predan J, Shan GX. Crack tip shielding or anti-shielding due to smooth and discontinuous material inhomogeneities. Int J Fract 2005;135:73–93. https://doi.org/10.1007/s10704-005-3944-5.
[95] Weichert D, Schulz M. J-integral concept for multi-phase materials. Comput Mater Sci 1993;1:241–8. https://doi.org/10.1016/0927-0256(93)90016-G.
[96] Yu H, Wu L, Guo L, Du S, He Q. Investigation of mixed-mode stress intensity factors for nonhomogeneous materials using an interaction integral method. Int J Solids Struct 2009;46:3710–24. https://doi.org/10.1016/j.ijsolstr.2009.06.019.
[97] Yu H, Wu L, Guo L, He Q, Du S. Interaction integral method for the interfacial fracture problems of two nonhomogeneous materials. Mech Mater 2010;42:435–50. https://doi.org/10.1016/j.mechmat.2010.01.001.
[98] Li W, Huang P, Chen Z, Yao G, Chen D. Single-side J-integral method for interfacial cracks. Int J Solids Struct 2022;241:111476. https://doi.org/10.1016/j.ijsolstr.2022.111476.
[99] Liu J, Wang Z, Kou J, Chen K. Synchrotron-based micro-laue diffraction for advanced functional materials: achievements and challenges. Photon Sci 2025. https://doi.org/10.1021/photonsci.5c00022.
[100] Yang W, Larson BC, Tischler JZ, Ice GE, Budai JD, Liu W. Differential-aperture X-ray structural microscopy: a submicron-resolution three-dimensional probe of local microstructure and strain. Micron 2004;35:431–9. https://doi.org/10.1016/j.micron.2004.02.004.
[101] Simons H, King A, Ludwig W, Detlefs C, Pantleon W, Schmidt S, et al. Dark-field X-ray microscopy for multiscale structural characterization. Nat Commun 2015;6:6098. https://doi.org/10.1038/ncomms7098.